Terrestrial Lidar Data Classification Based on Raw Waveform Samples Versus Online Waveform Attributes

Mohammad Pashaei, *Member, IEEE*, Michael J. Starek, *Member, IEEE*, Craig L. Glennie, *Member, IEEE*, and Jacob Berryhill

***Abstract*— In this study, the potential of raw samples of digitized echo waveforms collected by full-waveform (FW) terrestrial laser scanning (TLS) for point cloud classification is investigated. Two different TLS systems are employed, both equipped with a waveform digitizer for access to the raw waveform and online waveform processing which assigns calibrated waveform attributes to each point measurement. Point cloud classification based on samples of the raw single-peak echo waveform is compared with point cloud classification based on the calibrated online waveform attributes. A deep convolutional neural network (DCNN) is designed for the supervised classification. Random forest classifier is used as a benchmark to evaluate the performance of the proposed DCNN model. In addition, feature importance and temporal stability of the raw waveform samples versus the calibrated waveform attributes for point cloud classification are reported. Classification results are evaluated at two study sites, a built environment on a university campus and a coastal wetland environment. Results show that direct classification of the raw waveform samples outperforms classification based on the set of waveform attributes at both study sites. Results also show that the contribution of the range, as the only geometric attribute in the raw waveform feature vector, significantly increases the classification performance. Finally, the performance of the DCNN for filtering ground points to generate a digital terrain model (DTM) based on classification of the raw waveform samples is assessed and compared to a DTM generated from a progressive morphological filter and to real-time kinematic (RTK) GNSS survey data.**

***Index Terms*— Deep learning, full-waveform analysis (FWA), light detection and ranging (lidar), machine learning, point cloud classification, remote sensing (RS).**

I. Introduction

CONVENTIONAL terrestrial and airborne laser scanning (ALS) systems based on the Time-of-Flight (ToF) measurement principle, which are characterized as analog discrete return light detection and ranging (lidar) systems, have long been used for topographic mapping and other remote-sensing (RS) applications. For each emitted laser pulse, echo detection and time-of-arrival (TOA) estimation of the backscattered laser pulse are performed in real-time by analog devices. In discrete return systems, The estimation of the TOA is highly affected by range walk, i.e., the amplitude of echo pulse detected by the receiver frontend [1]. The analog estimators may yield significant range errors or completely fail in accurately detecting multiple targets along the laser transmit path, depending on the temporal separation between consecutive targets with respect to the emitted laser pulsewidth [2].

In contrast to discrete return systems, in echo-digitizing lidar systems, the complete return signal from the reflecting target is sampled at high rate and recorded in a digital form prior to performing the target detection [3]. Small footprint full-waveform (FW) ALS systems have been developed in the past few decades [4]. More recently, terrestrial, mobile, and unmanned airborne lidar systems with the capability of recording FW data are also becoming more readily available. Echo pulse attributes, such as amplitude and width, derived from the waveform signal backscattered from a reflecting object are shown to be useful for classification of lidar data collected over natural and built environments [5], [6].

However, extracting the fundamental properties of the returned waveform, such as the number of relevant peaks and parameters describing the shape of each detected echo in the waveform signal is a challenging task in signal processing [4]. Moreover, the echo pulse attributes need to be discriminative enough to be exploited as relevant features in the feature vector of the target for efficient classification. Depending on the employed FW lidar system for collecting waveform data, and the required accuracy to extract waveform attributes, different techniques have been developed for waveform decomposition and modeling [4], [7]. By carrying out a radiometric calibration procedure on waveform data, more relevant features can also be introduced to the feature vector of the target to improve the overall accuracy of the classification task [3], [5].

In some lidar systems, especially terrestrial laser scanning (TLS) systems, the system response model is usually unknown or too complex for modeling and decomposing the waveform using typical parametric functions, such as the well-known generalized Gaussian function [2]. To take the advantage of the capability of FW TLS systems in

Manuscript received September 1, 2021; revised November 3, 2021; accepted November 26, 2021. Date of publication December 3, 2021; date of current version March 29, 2022. This work was supported by the National Oceanic and Atmospheric Administration, U.S. Department of Commerce, prepared by Texas A&M University at Corpus Christi, using Federal Funds under Award NA18NOS4000198. *(Corresponding author: Michael J. Starek.)*

Mohammad Pashaei and Michael J. Starek are with the Department of Computing Sciences and the Conrad Blucher Institute for Surveying and Science, Texas A&M University at Corpus Christi, Corpus Christi, TX 78412 USA (e-mail: mpashaei@islander.tamucc.edu; michael.starek@tamucc.edu).

Craig L. Glennie is with the Department of Civil and Environmental Engineering, University of Houston, Houston, TX 77204 USA (e-mail: clglennie@uh.edu).

Jacob Berryhill is with the Conrad Blucher Institute for Surveying and Science, Texas A&M University at Corpus Christi, Corpus Christi, TX 78412 USA (e-mail: jacob.berryhill@tamucc.edu).

Digital Object Identifier 10.1109/TGRS.2021.3132356

digitizing and recording the return signal for classification tasks, an intensive calibration procedure for approximating the actual system response model seems inevitable [2], [8]. This approximated model will later be used as the basic template for waveform decomposition and modeling which can be accomplished, almost in real time, by an internal FW processing unit in some lidar systems [8], [9].

Due to the fact that digitized waveform samples are the fundamental source of data for modeling the waveform and extracting echo parameters, samples of the raw echo waveform may have the potential to be directly employed as waveform features representing physical characteristics of the illuminated target. One advantage of this approach is that conventional FW analysis (FWA) techniques are not required for extracting common waveform attributes. Therefore, uncertainties in evaluating the echo parameters due to the low capacity of the parametric functions for fitting to the echoes are eliminated. In addition, due to the lower sampling rate of the digitizer (usually 2 ns) and higher nonlinear system response in TLS systems, with respect to FW ALS systems, common FWA techniques are not usually applicable in a FW TLS system for the full dynamic range of the lidar system [2], [8].

II. Background

A FW lidar system is capable of digitizing and recording the complete temporal energy profile of the backscattered laser signal from the reflecting target, where the "waveform" is the term that refers to the shape of the echo signal [3]. In comparison to discrete-return lidar systems, the data collected by FW lidar systems contain additional information about the physical and spatial properties of the illuminated target in the footprint of the laser beam [4]. Specifically, in critical target situations where the target location with respect to the nearby targets or its spatial distribution along the travel path of the laser pulse causes uncertainty in range determination or target identification, analyzing the additional information may help to partly resolve those ambiguities [10]. This additional information is typically derived from detection and modeling of each individual echo within the digitized waveform signal. Two of the most important echo attributes include echo pulse amplitude, which is related to the radiometric characteristics of the target, and pulsewidth, which is a measure of the target-laser beam configuration and/or surface roughness at scales comparable to the laser wavelength [11]. These echo attributes and their derivatives, including the reflectance and geometry of the target with respect to the laser beam, such as the backscatter cross section and backscattering coefficient, have been widely used as relevant waveform features for target classification or segmentation [12], [13].

Analyzing the waveform, which encapsulates both radiometric and geometric properties of the illuminated target, is usually accomplished in an offline (or post-processing) mode using a pre-defined FWA technique [4]. Some lidar systems, however, such as Riegl VZ-Line TLS systems, offer an online waveform processing approach [2]. In this approach, the analysis of the returned waveform is carried out in real time, where the actual system response, derived from an intensive system calibration procedure accomplished by the lidar manufacturer, is exploited for waveform decomposition and modeling [2]. This is due to the fact that the tremendous dynamic range of the TLS system usually leads to a large degree of nonlinearity in the characteristics (e.g., scale) of the system response. However, by providing the raw digitized waveform data, Riegl VZ-Line scanners offer the enduser the flexibility to apply more in-depth and advanced analysis on the raw waveform data to achieve satisfactory results.

A. Waveform Features for Classification

The development of FW lidar systems and the advancement in FWA algorithms have brought interest to explore the suitability of features derived from digitized returned waveform signals for lidar data classification [13]–[16]. FW lidar data classification has been met through different approaches. Some work focus only on the geometric properties of targets and explores the most relevant geometric features describing different targets for classification. This approach emphasizes the improvement in geometric representation of the measured target for classification purposes. Improvements in the geometric representation of the target will help to better discriminate different targets in the classification procedure [17]–[19]. Other studies explore the combination of basic waveform features, such as the echo width and (uncalibrated) amplitude, with some calibrated attributes, such as the backscatter cross section or backscattering coefficient, derived from the echo waveform in the feature vector of the target [12]–[14], [20]. Some geometric features related to the targets in lidar data, such as elevation differences and surface normal, and features related to the position of a detected echo in the waveform or coefficients describing the deviation of the echo pulse from the ideal transmitted pulse may also be considered to enhance the classification performance [13], [21], [22]. The potential of parameters related to the structure of the waveform, such as the rise time to the first echo, ratio between tree canopy and ground energy, total waveform energy, and height of median energy have also been explored for airborne lidar data classification [23], [24].

Although the benefits of FW lidar data are particularly profound for forestry and vegetation segmentation due to its ability to provide accurate and detailed information about the vertical structure of the vegetated area and the terrain elevation underneath [25], [26], FWA has also been found advantageous for the challenging task of classification of natural and built objects in developed environments. Additional information about the reflecting properties of natural and built structures and their spatial distribution, encoded in the waveform data, have been shown to be relevant for land cover mapping and target classification in urban and natural areas [15], [21], [25], [27], [28]. However, in complex areas, the basic waveform features become less discriminative for a multiclass classification task [5], [13]. Nevertheless, some research studies have developed FWA techniques to derive more accurate basic features as well as some advanced features from the backscattered signal [12]. Studies have shown that employing basic and advanced waveform features along with careful radiometric calibration of the data improves multiclass

classification in urban areas [12], [13], [29]. Furthermore, adding features such as the total number of echoes within each waveform and the position of the echo in the waveform together with some geometric and/or spectral features derived from the lidar system or integrated sensors such as multispectral or hyperspectral cameras can significantly increase the accuracy of the multiclass classification of lidar data over complex environments [5], [22], [30], [31].

B. Objectives of This Work

This article seeks to investigate the utility of the samples of digitized raw waveform for multiclass classification of targets within built and natural environments. Classification performance is evaluated at two study sites: a university campus and a coastal wetland. Natural and made-made targets found in the selected study sites are classified through direct classification of the corresponding backscattered waveforms. The FW TLS systems employed in this study are equipped with online waveform processing capability and a waveform digitizer, which provides the enduser with digitized raw waveform for advanced post-acquisition analysis.

The hypothesis in this study is that the relevant waveform features for classification, either derived from the online waveform processing or in an offline mode using the post-processing FWA, are not always available. Moreover, in either case, samples of the digitized waveform are the primary source for waveform modeling and feature extraction. Thus, this study aims to investigate the potential of the raw samples of digitized single-peak echo waveforms for target classification. In this work, feature vectors containing samples of the raw digitized waveform are referred to as offline waveform feature (attribute) vectors. Spatial information-related neighboring targets are not included in the proposed classification approach. Due to the high correlation between the target's distance and the received optical energy by the lidar system, the range to the target is the only geometric feature which is included in the feature vector of the illuminated target. However, for the sake of completeness, the discriminative capability of samples of the waveform for multiclass classification in the absence of the range attribute will also be reported.

The potential of digitized raw waveform samples is compared with the capability of calibrated waveform features, derived from the online waveform processing, for target classification. The calibrated waveform features are referred to as the online waveform features throughout this article. Due to the importance of single-peak echo waveforms in representing geophysical characteristics of targets, where the calibrated parameters directly relate to the spatial and radiometric properties of the illuminated target, only waveform samples related to single-peak echo waveforms are considered for waveform classification and feature analysis. In addition, as it has been explained in Section V, the majority of waveform data collected at each study site is single-peak echo waveforms. For the sake of fairness in the comparative analysis, only the online waveform attributes related to single-return measurements are considered for classification.

At the built environment (campus) study site, online and offline waveform attributes in the feature vectors are analyzed for classification using FW TLS datasets collected at two different points in time. Each individual dataset includes multiple scan positions within the same environment. Employing these datasets is crucial for investigating the robustness of the suggested point cloud classification approach. First, by having multiple scan positions within one dataset, the training and testing of the classifier can be carried out on two separately collected datasets. Second, collecting FW TLS data from multiple scan positions significantly decreases the correlations between a certain target category and some properties of the measured waveform that are highly correlated with the TLS-target geometric configuration, such as the range to the target. Finally, two waveform datasets collected at two different points in time from the same study area makes it possible to perform a temporal stability analysis on both online and offline waveform feature vectors.

At the natural environment (wetland) study site, classification is performed using a different FW TLS system than that used in the built environment, but manufactured by the same company. This TLS is also equipped with online waveform processing and a waveform digitizer. This study site provides an additional evaluation of the robustness of the raw waveform classification approach within natural terrain and based on a different TLS system.

The main contributions of this article are as follows.

1) Classification performance on raw waveform data is compared with classification based on online waveform attributes (features) derived from a calibrated lookup table (LUT) provided by the TLS system manufacturer.
2) A deep convolutional neural network (DCNN) architecture is developed and employed for the multiclass classification task, where the offline (raw waveform data) and online waveform feature vectors related to each target are used as input to the DCNN model. Furthermore, the classification performance of the DCNN model is compared with that from a random forest (RF) model and important features in both online and offline waveform feature vectors are reported.
3) Temporal stability of the offline versus online waveform features for classification is investigated through evaluating the classification performance on two datasets collected at two different points in time.
4) Task evaluation of the DCNN for filtering ground points to generate a digital terrain model (DTM) of the wetland surface based on online and offline waveform feature vectors is performed.

The remainder of this article is organized as follows: Section III describes online and offline FWA. Section IV introduces the study sites and collected FW TLS data. The methodology employed for FW TLS data classification and evaluation based on raw and online waveform attributes is presented in Section V. Results are presented and discussed in Section VI. Finally, Section VII concludes with some future work considerations.

III. FWA Approaches

A. Offline FWA

Offline FWA, which is usually employed in FW ALS systems is a post-processing approach to detect pulses and related attributes, e.g., amplitude, and width from the digitized echo signal. Those echo pulse attributes can later be used to derive some information about the scattering characteristics of the illuminated targets. Different approaches proposed to extract the target backscattering properties encoded in the digitized waveform can be broadly categorized into two main approaches: 1) deconvolution-based methods [7] and 2) methods based on fitting the digitized echo waveform with basic parametric functions [3]. With the assumption that the system response can be described and modeled with an ideal Gaussian function, which is usually true in FW ALS systems with limited dynamic range, Gaussian decomposition and modeling has become a widely accepted FWA approach in FW ALS systems [3], [21], [25]. However, applying Gaussian decomposition and modeling on FW data collected from FW TLS systems, with a large dynamic range, usually leads to unsatisfactory results [8].

B. Online FW Processing

Since 2008, Riegl Laser Measurement Systems, GmbH, Horn, Austria, has developed a line of lidar systems, commonly called V-Line, based on pulsed ToF technology with real-time echo digitization and online waveform processing capabilities [9]. Indeed, Riegl V-Line lidar systems combine the advantages of analog detection systems, in which lidar survey results are provided without the need for post-processing, with those of airborne echo digitizing lidar systems [1]. In contrast to FW ALS systems, in which digitized returned waveforms are stored during flight for FWA in an offline or post-processing mode, the lack of computational power in TLS systems for real-time processing has led Riegl to implement online waveform processing for V-Line scanners including VZ-Line TLS products [1].

As opposed to FW ALS systems in which an ideal Gaussian pulse, usually, closely approximates the sensor's system response, the Riegl VZ-Line systems exploit the actual sensor's system response derived from an intensive calibration procedure performed by the manufacturer [2]. This actual system waveform is employed for the waveform decomposition and derivation of physical observables describing the scattering properties of the target, such as the target's laser cross section or calibrated relative reflectance, within an automatic procedure called online waveform processing [2], [8]. In this approach, the nonlinear scale characteristics of the system response are perfectly captured by the calibrated sensor's system response, resulting in the utmost accuracy and precision in the echo decomposition and reconstruction [2], [8]. In addition to calibrated relative reflectance, the online waveform processing in VZ-Line TLS systems provides calibrated amplitude and pulse deviation for each detected echo signal.

1) Calibrated Amplitude: The amplitude of the optical echo signal detected in the receiver depends on a number of factors including system-related factors, such as emitted laser pulse and the receiver aperture, and target-related factors, such as target's laser radar cross section which is a function of the target's reflectance in the laser's wavelength, target's size, and the directivity of the target's reflection [9]. By means of a precise calibration procedure during manufacturing, the amplitude of every detected pulse is given relative to the amplitude of an echo signal at the detection threshold of the lidar system as [9]

$$A_{\mathrm{dB}} = 10 \times \log\left(\frac{P_{\mathrm{echo}}}{P_{\mathrm{DL}}}\right) \tag{1}$$

where A_{dB} is amplitude in decibel, P_{echo} is the optical input power, and P_{DL} is the minimum detectable input power. The logarithmic measure, given above, covers the wide dynamic range of the employed TLS system. However, the amplitude of the echo signal, detected by the receiver, is highly correlated with the range value making it difficult to discriminate different targets based purely on their amplitude readings for target classification.

2) Calibrated Relative Reflectance: The target reflectance is a physical target property, which refers to the fraction of the incident laser's optical power that is reflected by the target at the laser wavelength. However, the reflected optical power measured at the receiver is highly correlated with the target range. The calibrated relative reflectance is defined as the ratio of the absolute amplitude of the target to the amplitude of a target of known reflectance at the same range, orthonormal to the laser beam and with a size larger than the laser footprint [9]. The target of the known reflectance is usually a white diffuse target with the reflectance of about 100%. This quantity relates the echo intensity to the target reflectance independent of the range to the target. The Riegl VZ-Line TLS systems take also the directivity of the target reflectance into account, making the relative reflectance comparable with the normalized laser radar cross section. The relative reflectance in dB, ρ_{rel}, measured by the lidar system is evaluated as [9]

$$\rho_{\mathrm{rel}} = A_{\mathrm{dB}} - A_{\mathrm{dB,Ref}}(R) \tag{2}$$

where A_{dB} is the calibrated amplitude and $A_{\mathrm{dB,Ref}}(R)$ is the calibrated amplitude of the reference target at range R.

3) Pulse Deviation: Online waveform processing in VZ-Line systems provides information about the pulse shape figure, where the shape of the echo pulse is compared with the expected (and undistorted) pulse shape for each individual echo pulse. In fact, pulse deviation represents the deviation of the returned pulse from the actual system response already evaluated and stored in the instrument [1]. The stored calibrated system response model, which encompasses the entire dynamic range of the TLS system, captures a large portion of systematic changes in the echo shape as a function of range, enabling accurate fits to the waveform [8], [9]. However, even the ideal echo signal, backscattered from an extended flat target orthonormal to the laser beam, still shows discrepancies with the stored system response [9]. This deviation especially increases for overlapping echoes, returning

Fig. 1. Co-registered TLS point cloud of the campus. Side view is colored gray by reflectance. (Left) Top view is color-coded by height. Circles show six TLS positions in the October survey. White circles represent two TLS positions for the July survey.

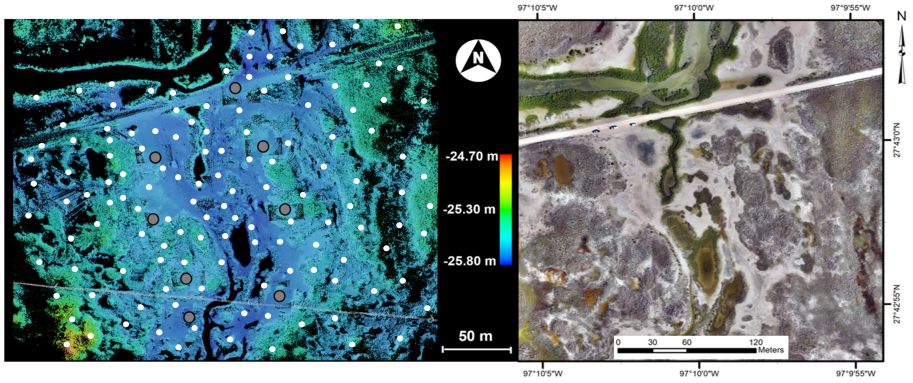

Fig. 2. Georeferenced point cloud collected from the coastal wetland, color-coded based on ellipsoidal height. The gray and small white circles represent the TLS positions and collected RTK GNSS points, respectively. The orthoimage on the right shows the land cover of the study site.

from targets located at a distance smaller than the multitarget resolution (MTR) distance (for example, 0.8 m in the Riegl VZ-400 TLS systems), and for broadened echoes returning from slanted targets [9]. The pulse deviation is given as [9]

$$\delta = \sum_{i=1}^{N} |s_i - p_i| \tag{3}$$

where N is the number of samples in the digitized echo signal with digital number (DN) value s_i, and p_i is the DN corresponding to the sample from the equivalent system response.

IV. Study Sites and Data

A. Study Sites

To perform this experiment on a built environment, part of the campus of Texas A&M University-Corpus Christi, TX, USA, was selected. The campus area includes natural and man-made structures such as palm trees, grass fields, asphalt roads, and buildings, which are used as target categories for classification. To evaluate the potential of the raw waveforms to discriminate tree canopy from grass fields, the tree category is divided into two separate subclasses (trunk and canopy) in the classification process, described further below. Fig. 1 illustrates the campus study site with the area of 94 600 m^2 displayed in two different views of the co-registered point cloud dataset collected by the Riegl VZ-400 FW TLS system at two different points in time.

The second study site, Mustang Island Wetland Observatory (MUI), is part of a coastal wetland located on a barrier island along the southern portion of the Texas Gulf Coast, USA, bounded by Corpus Christi Bay to the west and the Gulf of Mexico to the east. Two prominent target categories in the selected coastal wetland are vegetated land cover and tidal flat areas. Tidal flat areas are bare-earth sediment surfaces, usually devoid of vegetation, and alternately submerged and exposed to the air by changing tide and water levels. In this study, tidal flat areas include exposed, lower lying, and tidal inundated wetland surface areas as well as exposed, upland and periodically inundated wetland surface areas within zones of vegetation cover. The vegetated areas include densely vegetated areas and areas with sparse vegetation cover. Some other target categories found in this study site include a dirt road and power lines. Thus, tidal flat, vegetation, road, and power lines are used for multiclass classification of this natural environment. Fig. 2 illustrates the coastal wetland study site with the area of 185 430 m^2 visualized with a georeferenced point cloud collected at 8 different scan positions with a Riegl VZ-2000i FW TLS.

It should be emphasized that, in each study site, targets with dominant observations have been considered for classification. Because the main purpose of this work is to assess the quality of information carried by the raw echo waveform without waveform modeling and calibration, main target categories describing the majority of the built study site in campus area are examined. In coastal wetland, however, due to the need for discriminating terrain points from above-ground objects for modeling the wetland topography, the exposed terrain surface and dominant vertical structures found in the study area, i.e., vegetated areas, and power lines are classified. Although there

TABLE I
TECHNICAL SPECIFICATIONS OF THE RIEGL VZ-400 AND VZ-2000I

TLS system	FOV	Max. Measurement range (Long range mode)	Measurement rate	Beam divergence	Laser wavelength	Angular resolution	Range accuracy	Range precision
VZ-400	$360^\circ \times 100^\circ$	for natural targets: $\rho \geq 20\%$ up to 280 m $\rho \geq 80\%$ up to 600 m	42 000 meas /sec (Long range mode) 122 000 meas /sec (High speed mode)	0.3 mrad	1550 nm	0.0005°	5 mm	3 mm
VZ-2000i	$360^\circ \times 100^\circ$	for natural targets: $\rho \geq 20\%$ up to 1300 m $\rho \geq 90\%$ up to 2500 m	21 000 meas /sec (Long range mode) 500 000 meas /sec (High speed mode)	0.3 mrad	1550 nm	0.0005°	5 mm	3 mm

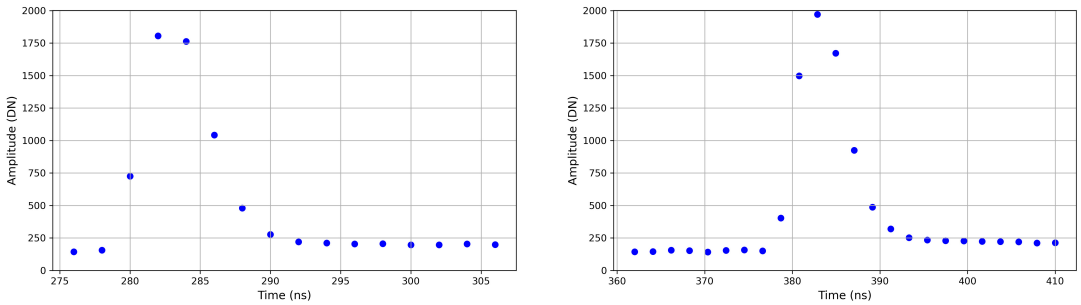

(a) (b)

Fig. 3. Single-peak digitized echo waveforms with 2-ns spacing measured by (a) Riegl VZ-400 and (b) Riegl VZ-2000i TLS generated from laser pulse returns from extended targets with similar reflectance values.

might be different vegetation types, classifying vegetation type is not the main purpose of this work. Thus, all vegetation types are classified under the same category.

B. FW TLS Data

The Riegl VZ-400 and VZ-2000i FW TLS systems were employed for collecting data from the campus and wetland study sites, respectively. Specifications of both lidar systems are given in Table I. These TLS systems not only perform online waveform processing, but also digitize and record the entire echo waveform at a sampling rate of 500 MHz or one sample per 2 ns. Fig. 3 illustrates single-peak digitized echo waveforms recorded by the Riegl VZ-400 and VZ-2000i from extended targets with the same reflectance values of about -3.2 dB derived from the online waveform processing. According to the figure, the Riegl VZ-400 TLS system records 16 samples related to the echo waveform while the Riegl VZ-2000i TLS system records 24 samples. Both cases are for an extended target perpendicular to the path of the emitted laser beam. However, both systems use the same digitization rate; the time separation between two consecutive samples in each individual waveform is 2 ns.

1) Campus Study Site: Two separate FW TLS surveys, performed at two different times using a Riegl VZ-400 TLS system, over the selected campus area have been considered for FW data classification. The first TLS survey was carried out on July 14, 2020, at two different scan positions. The second survey was carried out on October 31, 2020, at six scan positions, where two of those scan positions were located at the same TLS positions and heights used to acquire data on July 14. The average temperature and humidity during data collection on July 14 are 37 °C and 78% and on October 31 are 20 °C and 55%, respectively.

In Fig. 1, the side view shows a TLS point cloud colored by calibrated relative reflectance values, while the top view represents the same point cloud data color-coded according to height. Circles in Fig. 1 show the scan positions in the collected datasets on October 31, where the two white circles show the TLS positions in common with the TLS survey conducted on July 14. The dataset collected on October 31 is used for training and testing the classifier. Having several scan positions for the October dataset is crucial for the robustness of the suggested classification approach. First, by having multiple scan positions within the study area, instances for training and testing the underlying classifier can be chosen from separate scan positions or a combination of them. Second, collecting FW TLS data from multiple scan positions significantly decreases the correlations between the shape of the return waveform and the geometric configuration of the target with respect to the TLS system. Furthermore, the trained classifier on the October dataset is also used to classify the dataset collected on July 14, which enables analysis of the temporal stability of online and offline waveform feature vectors for classification.

For both TLS surveys, point cloud/waveform data were collected at each scan position in panoramic mode with a 360° horizontal field-of-view (FOV) and 100° (from -40° to $+60^\circ$) vertical FOV using the scanner's high-speed acquisition mode with FW recording turned on. The pulse repetition rate (PRR)

was set to 300 kHz, corresponding to 122 000 measurements per second, and the minimum step angle was set to 0.0024° equivalent to 4-mm point spacing at 100 m.

Registration and fine alignment of individual scan positions into a cohesive point cloud was performed with Riegl RiSCAN PRO, version 2.12.1, software package, using the multistation adjustment (MSA) plugin. MSA results reported by the RiSCAN PRO software show the final horizontal and vertical accuracy of TLS scan co-registration are 0.006 and 0.004 m, respectively, with angular precision better than 0.004° for all angular parameters. Registered point cloud data from both TLS surveys was locally referenced within a project oriented coordinate system.

2) Wetland Study Site: The TLS survey of the wetland study area was conducted on February 23, 2021, at eight different scan positions using the Riegl VZ-2000i FW TLS with an integrated real-time kinematic (RTK) GNSS receiver. The average temperature and humidity during data acquisition in the coastal wetland area are 24 °C and 56%, respectively. Fig. 2 illustrates the TLS locations on wetland study site using gray circles on the georeferenced point cloud color-coded based on ellipsoid height. The orthoimage given in Fig. 2 shows the land cover within the wetland study site. Point cloud and digitized waveform data were collected at each scan position in panoramic mode with a 360° horizontal FOV and 100° (from −40° to +60°) vertical FOV using the scanner's high-speed acquisition mode. The PRR was set to 600 kHz, corresponding to 250 000 measurements per second, and the minimum stepping angle was set to 0.0024°.

The scan positions were co-registered using the same procedure described above for the campus study site and georeferenced based on the VZ-2000i's integrated RTK GNSS receiver, which received corrections from the Texas Department of Transportation (TxDOT) real-time network (RTN) during data acquisition. This approach provided absolute positional accuracy down to a few centimeters. Spatial referencing was set to the North American Datum of 1983 (NAD83), National Adjustment 2011, State Plane Coordinate System, Texas South Zone for the horizontal point cloud coordinates. Vertical coordinates were referenced to the NAD83 ellipsoid. Georeferencing of the TLS data at the wetland site was necessary for assessment of waveform classified ground point data for DTM generation and comparison to RTK survey data, described further below.

C. RTK GNSS Control Points on Coastal Wetland

A network of 132 RTK GNSS points was collected on the bare-earth surface in the coastal wetland study site using an Altus NR3 (Septentrio) RTK GNSS rover with cellular-based corrections provided by the TxDOT RTN (see Fig. 2). Coordinates at each sample point were computed from a 10-s observation average at 1-Hz sample rate. Ellipsoidal height (vertical) accuracy using this procedure is estimated to be within 2.7 cm ($1\,\sigma$). All RTK data were collected in the same reference frame as the TLS survey.

These RTK points serve as ground truth (i.e., vertical control points) for evaluating DTMs generated from the offline and online waveform classified point cloud data explained later in this article. RTK points were distributed throughout the study area, collected on surfaces within vegetated and exposed land cover. From the total set of collected control points, 30 points represent hard surfaces, including tidal flats and dirt road areas, and the remaining 102 points characterize vegetated areas, including both densely vegetated areas and areas with sparse vegetation. RTK GNSS points collected on hard surfaces are used to evaluate the vertical accuracy of the TLS data.

V. Methodology

For the purposes of this work, a filtering procedure must first be implemented on all collected TLS datasets to extract single return points derived from online waveform processing and corresponding single-peak echo waveforms. In addition, for a multiclass supervised classification task, an appropriate number of ground-truth instances need to be generated for both study sites.

A. Single-Peak Echo Waveforms

The Riegl RiSCAN PRO, version 2.12.1 software package was used for visualizing, filtering, and exporting the point cloud derived from the online waveform processing with selected attributes. Riegl also provides a software toolkit called RiWaveLib library for advanced research and analysis purposes on the raw waveform data acquired by the Riegl VZ-Line scanners. The digitized echo waveform corresponding to a selected point in the point cloud is accessible through the timestamp attribute assigned to that point, derived from the online waveform processing.

The point cloud data collected from each scan position is filtered to include points related to the single-peak echo waveforms. Such filtering is necessary because the radiometric calibration of the lidar instrument and the resulting relative reflectance are valid for extended targets. In other words, radiometric calibration in a lidar system assumes that the received intensity values are from a single target with a size larger than the footprint of the laser beam. Moreover, due to the higher variations in the echo shape caused by the influence of central obscuration for targets measured at a close range to the scanner [32], [33], especially up to 9 m [8], the single-peak echo waveforms and corresponding points in the point cloud data, at both study sites, are also filtered to exclude data points collected at distances less than 9 m from the TLS instrument. The net result of the filtering procedure is the exclusion of about 8% and 15% of the waveforms collected from the campus and coastal wetland study sites, respectively.

The point attributes exported from the Riegl RiSCAN PRO software include the 3-D coordinates, range to the scanner, calibrated amplitude, calibrated relative reflectance, and pulse deviation. For the sake of simplicity, amplitude and reflectance are used rather than calibrated amplitude and calibrated relative reflectance, respectively, in the remaining sections of this article. The 3-D coordinates are not included in the classification process but they are employed for visualization purposes.

TABLE II

TOTAL NUMBER OF GROUND-TRUTH INSTANCES GENERATED FROM THE TWO COLLECTED DATASETS OVER THE CAMPUS STUDY AREA. FOR EACH DATASET, THE NUMBER OF GROUND-TRUTH INSTANCES RANDOMLY SAMPLED FOR TRAINING AND TESTING IS GIVEN

Dataset	Point cloud / Raw waveform	Asphalt	Building	Grass	Tree trunk	Tree canopy
October	59,470,887	25,639,548	20,179,562	7,391,730	1,711,501	4,548,546
July	12,112,869	3,530,778	3,009,509	2,094,158	1,419,761	2,058,663
Training (October)	1,000,000	200,000	200,000	200,000	200,000	200,000
Testing (October)	20,000,000	6,500,000	6,500,000	3,600,000	1,000,000	2,400,000
Testing (July)	5,500,000	1,700,000	1,900,000	655,000	385,000	860,000

TABLE III

TOTAL NUMBER OF GROUND-TRUTH INSTANCES GENERATED FROM THE COLLECTED DATASET OVER THE COASTAL WETLAND STUDY AREA. FOR EACH DATASET, THE NUMBER OF GROUND-TRUTH INSTANCES RANDOMLY SAMPLED FOR TRAINING AND TESTING IS GIVEN

Dataset	Point cloud / Raw waveform	Tidal flat	Vegetation	Road	Power line
Coastal wetland	18,181,280	10,862,557	5,796,947	1,085,289	436,487
Training	800,000	200,000	200,000	200,000	200,000
Testing	17,381,280	10,662,557	5,596,947	885,289	236,487

To explore recorded waveform data, computer programs were developed using the software library RiWAVELib, and compiled with Microsoft Visual C++ on Windows platform. Examining the single-peak echo waveforms acquired by the Riegl VZ-400 TLS system shows that more than 98% of waveforms contain 16 or 24 samples (DNs). The same examination on the single-peak echo waveforms collected by the Riegl VZ-2000i TLS system shows that more than 97% of the single-echo echo waveforms contains 24 or 32 samples. Echo waveforms with more than 24 samples recorded by the Riegl VZ-400 or waveforms with more than 32 samples measured by the the Riegl VZ-2000i usually belong to highly inclined surfaces in the path of the laser beam or are a consequence of merged echoes from targets spaced closer than the target separation resolution of the lidar sensor. Thus, to avoid including those waveforms in classification procedure, those waveforms are filtered out from the related dataset.

B. Ground Truth for Classification

Ground-truth instances were generated from the data collected at all scan positions in each study site by careful inspection of the acquired point cloud and manual selection of points related to the desired target.

1) Campus Study Site: The total number of ground-truth points and corresponding waveform instances generated from the filtered dataset collected by the Riegl VZ-400 TLS over the campus study site in October and July are given in Table II. From the total number of points in the filtered October dataset, 1 000 000 ground-truth points with online waveform features and corresponding waveforms were randomly selected for training the classifier, where each target category participates in training the classifier with 200 000 random point and waveform instances. The number of randomly selected points and related waveforms from the October dataset, used for testing the classification performance is given in Table II. It is worth noting that the training and testing sets do not include shared instances. Table II also reports the number of points and corresponding waveform instances for testing the classifier on the July dataset after training using the October dataset.

2) Wetland Study Site: Ground-truth instances generated from the filtered dataset collected by the Riegl VZ-2000i TLS system over the coastal wetland area are given in Table III. It summarizes the total number of generated ground-truth points and corresponding waveforms, and the number of instances that belong to each target category, for training and testing of the underlying classifier. According to the table, for each target category, 200 000 point and waveform instances were randomly selected from the total number of generated ground-truth instances.

C. Online Versus Offline Waveform Feature Vectors

For both TLS systems used in this study, the online waveform feature vector related to each individual single-return point instance includes the range to the scanner, amplitude, reflectance, and pulse deviation. The corresponding single-peak offline waveform feature vectors, however, have different lengths for each TLS system. The offline waveform feature vector includes the range value and a series of 24 DNs for the waveforms measured by the Riegl VZ-400 TLS system, while for the VZ-2000i TLS systems the feature vector includes 32 DNs and range value. The missing elements in offline waveform feature vectors constructed on digitized waveforms with the length shorter than 24 and 32 samples measured by Riegl VZ-400 TLS and Riegl VZ-2000i TLS, respectively, are filled by the DN representing the value of the last sample of the measured waveform. It should be recalled that no pre-processing step, such as waveform modeling using parametric functions for extracting typical waveform features, has been applied on digitized echo waveform. As mentioned earlier, the range value is the only geometric attribute which is included in both online and offline feature vectors. It is assumed that the dependency of the intensity to the range from

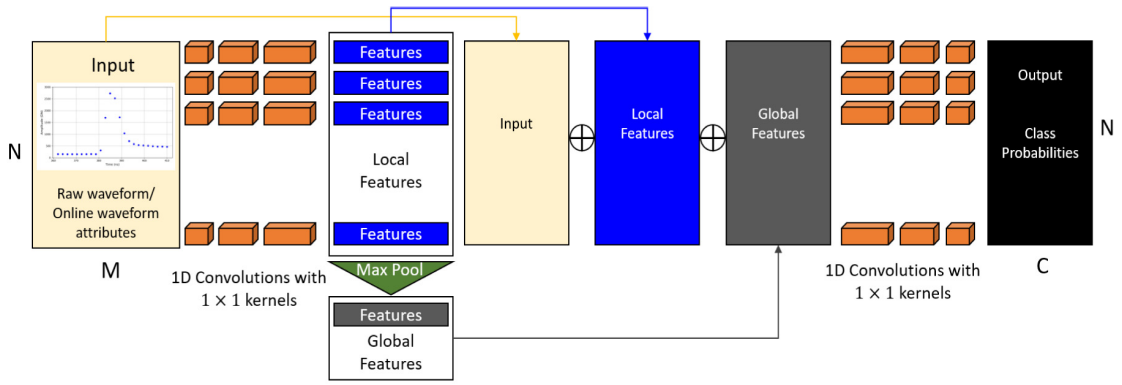

Fig. 4. Proposed DCNN architecture for FW TLS data classification.

the target, which is resolved during radiometric calibration of the echo waveform signals, can be partially captured by the classification algorithm when the classifier is trained on feature vectors including the range attribute. However, for the sake of completeness, the same feature vectors excluding the range attribute are also used for training and validating the same classifiers.

D. DCNN Architecture for FW TLS Data Classification

DCNN architectures have significantly outperformed almost all traditional machine learning (ML) approaches for classification and segmentation tasks in an end-to-end manner [34]. Although a large number of DCNN architectures have been developed for 3-D point cloud classification and segmentation, the potential of a DCNN architecture has not yet been fully explored, to the best of the author's knowledge, for 3-D point cloud classification based on the raw waveform samples or waveform-derived attributes through a FWA technique, related to each individual point in the point cloud [28], [34], [35]. Moreover, most of recently proposed DCNN architectures for point cloud classification try to explore features describing the geometric relationship of a 3-D point with other points in both a local and a global extent for point cloud classification or segmentation [34]. This is not the case in our experiment, where points are classified based only on their raw waveform samples or calibrated waveform-derived attributes.

The proposed DCNN architecture for FW TLS data classification, developed as part of this study, is shown in Fig. 4. The input to the network is a matrix of data of size $N \times M$, where N is the number of input instances that are simultaneously fed to the network for classification and M is the number of elements in the input vector. For example, for the offline waveform feature vector classification over campus study site, the input vector includes $M = 25$ elements, in which 24 elements represent 24 samples of the digitized waveform measured by the Riegl VZ-400 FW TLS system and the remaining element represents the recorded range to the target. In the case that the online waveform feature vectors are fed to the network for classification, M is equal to 4, where the first three elements represent three online waveform attributes (i.e., amplitude, reflectance, and pulse deviation) related to the measured target and the range value.

According to Fig. 4, the first block of the proposed DCNN architecture takes the input data and computes the local features for each input vector using three 1-D convolutional kernels of size 1×1 with batch normalization. Each convolutional layer is then followed by a nonlinear activation function, such as ReLU:

$$f(x) \approx \mathrm{ReLU}(\mathbf{W}x + \mathbf{b}) \tag{4}$$

where x is the input vector or the feature vector computed in an earlier convolutional layer, $\mathbf{W}$ is the learnable weight parameters, and $\mathbf{b}$ is bias parameter.

Local features derived in the first convolutional block are fed into a max pooling layer to extract global features from the input feature vectors. As a symmetric function, max pooling layer produces the same output feature vector without any dependence on the order of the input data. The second part of the network concatenates the input vector with both the local and global feature vectors and the resulting vector is fed to the second set of convolutional layers, where three 1-D kernels of size 1×1 with batch normalization and the ReLU activation function is applied on each individual input feature vector. To solve the classification of the input data, the feature vector resulting from the last convolutional layer is fed into the classifier defined on top of the DCNN architecture, where the class probability is calculated for each individual input vector by the softmax layer as

$$p_i = \frac{e^{y^i}}{\sum_{j=1}^{C} e^{y^j}} \tag{5}$$

where p_i is the class probability of the class i with output value of y^i and C is the total number of classes.

Furthermore, due to the fact that collected FW TLS data may include severe imbalanced instances in different classes, the DCNN model uses the weighted categorical cross-entropy loss for training. The loss function can be formulated as

$$\mathcal{L}_{\mathrm{CE}} = \sum_{n=1}^{N} \sum_{c=1}^{C} W_c t_{n,c} \log\left(\mathcal{Y}_{n,c}\right) \tag{6}$$

where, $\mathcal{L}_{\mathrm{CE}}$ is the categorical cross-entropy loss, $t_{n,c}$ is the ground-truth value in one-hot vector representation, and $\mathcal{Y}_{n,c}$ is the value showing the predicted probability of class c for

the input vector n. W_c is the weight for class c, which can be defined as

$$W_c = \frac{1}{\ln\left(1.2 + \frac{a}{b}\right)} \tag{7}$$

where a is the number of the instances of the same target category and b is the total number of instances in all target categories.

In this classification experiment on FW TLS data, the first set of convolutional layers include 256, 512, and 1024 filters, ending with a bottleneck layer of dimension 1024. Also, the second set of the convolutional layers include three sets of 1024, 512, and 256 filters, ending with a bottleneck layer of dimension 256. To train the DCNN model, the learning rate α was set to 0.001, and Adam optimizer [36] was chosen for updating weights during training. Two exponential decay rate parameters in the Adam optimizer β_1 and β_2, were set to 0.9, and 0.999, respectively. ϵ parameter in the optimization algorithm was set to 1×10^{-7} to avoid any division by zero. The experiment was carried out with 300 epochs on Google Colab, Google's free cloud service, with one Intel(R) Xeon(R) CPU 2.30 GHz and one high-performance Tesla $K80$ GPU, having 2496 CUDA cores and 12-GB GDDR5 VRAM.

E. Random Forest for FW TLS Data Classification

To compare the performance of the proposed DCNN architecture for FW lidar data classification with a traditional ML-based classification approach, a random forest (RF) classifier is employed. The RF algorithm is an ensemble ML technique which uses a large number of tree-like classifiers in the ensemble and achieves a classification accuracy comparable to boosting technique. RF is a very robust classifier against overfitting the training data and does not require any assumptions about the distribution of the data. Furthermore, due to its ability to handle big, unbalanced, and high-dimensional data, it is one of the most popular ML techniques for supervised classification of RS data, including hyperspectral imagery and lidar data [22], [37]. In addition, the RF classifier estimates the importance of each feature in the feature vector of the training instances. This capability can be exploited to find the most discriminative features in both online and offline feature vectors.

Although RF classifier is not sensitive to the user-defined values for hyperparameters, in this study, the grid search method along with the fivefold cross-validation (CV) technique was employed to find the best settings for the hyperparameters. The trained classifier is then used to evaluate the classification performance on two separate test sets given in Table II. The best hyperparameter settings found for efficiently training the RF classifier over the campus dataset include 500 trees with a maximum depth of 20 for online waveform feature vectors and 1000 trees with a maximum depth of 50 for offline waveform feature vectors. The maximum number of features for splitting a node, minimum number of samples required for splitting a node, and minimum number of samples required in a leaf are 2, 2, and 2, respectively, for training the RF classifier with both online and offline waveform feature vectors. In addition, both RF classifiers use the bootstrap technique for sampling data points during training and testing.

F. Point Cloud Filtering for DTM Generation

Discrimination between the ground and above-ground targets is one of the most interesting, yet challenging topics in the applications of lidar data, including TLS, for generating accurate an DTM in natural environments. In this work, classified TLS point cloud data collected at the coastal wetland study site are used to filter ground points from above-ground objects and subsequently generate a DTM of the wetland ground surface. To do so, the point cloud data classified by the online and offline waveform features using the proposed DCNN classifier are simply filtered according to their predicted label. The resulting filtered datasets include points related to the tidal flat and dirt road areas within the study site, which are collectively called hard surface areas for the purposes herein. Those datasets are later used to generate the DTM model.

To evaluate the accuracy of the DTM generated from DCNN-based classification, a baseline ground point set is generated using the well-known progressive morphological filter (PMF) proposed by Zhang *et al.* [38]. The accuracy of the PMF filtering result is evaluated by computing the vertical distance from a triangulated irregular network (TIN) model generated from the PMF classified ground point set to the RTK GNSS points. The PMF DTM is then used to evaluate the accuracy of the DCNN-based classification of hard surface points, and subsequent DTM, based on online and offline waveform features.

VI. Results and Discussion

A. Built Environment Classification Using Online Waveform Features From the October Test Set

Fig. 5 visualizes the distribution of online waveform features for each target category from the online waveform feature vectors of the October dataset and Table IV summarizes some statistics related to these features. It is worth noting that for better visualization of the feature distributions given in Fig. 5, the upper bound of the X-axis in each plot is limited to the feature value that covers the distribution of 99.5% of the data.

For almost all target categories shown in Fig. 5, the distribution of each feature has overlap with features in other target categories. This usually leads to high interclass similarity for underlying target categories and consequently a decrease in classification performance. Referring to the figure, the range distribution plot shows a large overlap for all target categories. This plot simply shows that no specific target can be correctly classified based solely on its range from the scanner. The distributions for calibrated amplitude also show high overlap for different target categories. However, the asphalt and grass classes show narrower amplitude distributions than the other targets. Building and tree trunk classes show the largest overlap in their amplitude distribution. In addition, asphalt and tree canopy show the largest overlap in amplitude distributions.

It should be noted that the amplitude feature given by the online waveform processing is not calibrated with respect to the range in comparison to relative reflectance, and as such,

TABLE IV

SUMMARY OF STATISTICS FOR ONLINE WAVEFORM FEATURES IN THE TRAINING DATASET. EACH COLUMN GIVES THE MINIMUM, MAXIMUM, MEAN, AND STANDARD DEVIATION OF THE RELATED FEATURE FOR THE UNDERLYING TARGET

Target	Range (m)	Amplitude (dB)	Reflectance (dB)	Pulse deviation
Asphalt	8.00, 199.70, 22.41, 15.10	0.34, 45.06, 23.77, 3.76	−20.07, 3.44, −7.64, 1.41	−1.00, 344.00, 7.43, 10.20
Building	13.61, 200.00, 48.56, 36.49	0.43, 43.73, 23.79, 6.01	−20.16, 2.49, −2.10, 1.68	−1.00, 311.00, 4.65, 4.13
Grass	8.35, 200.00, 23.93, 21.04	0.63, 35.59, 27.06, 4.33	−20.14, 5.79, −4.23, 1.46	−1.00, 400.00, 32.45, 37.56
Tree trunk	9.10, 200.00, 44.75, 31.93	0.40, 34.56, 26.27, 5.75	−20.06, 2.14, −2.17, 1.40	−1.00, 381.00, 3.70, 3.82
Tree canopy	8.56, 200.00, 42.83, 30.69	0.48, 35.36, 19.56, 6.28	−20.35, 3.33, −7.39, 2.98	−1.00, 422.00, 30.64, 43.75

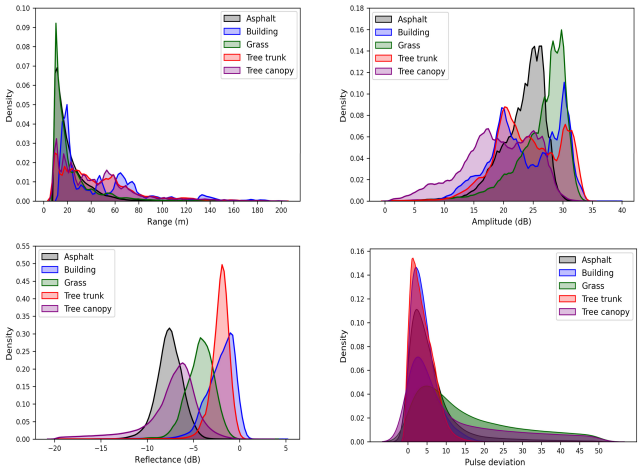

Fig. 5. Distribution of the online waveform features for different targets in the training dataset.

the amplitude feature shows wider distributions and higher overlaps for almost all target categories. The plot representing the distribution of pulse shape, also, shows large overlap areas for different targets. Distributions of relative reflectance show the highest separability among different target categories with respect to the other online waveform features. That is expected due to the careful radiometric calibration of the TLS system by the manufacturer. However, different targets still show considerable overlap for reflectance values. The most noticeable overlaps are between asphalt and tree canopy classes and also between tree trunk and building classes. Furthermore, except for the relative reflectance, the other online waveform features represent multimodal distributions.

Distributions of the reflectance attribute and its mean values for each individual target category, given in Fig. 5 and Table IV, respectively, show its important role in separating asphalt and tree canopy from the building and tree trunk classes. It also helps to discriminate grass from all other target categories. Referring to the statistics reported in Table IV, mean reflectance shows comparable values between asphalt and tree canopy classes and also between building and tree trunk classes, making this feature less discriminative for instances in those target categories. Furthermore, pulse deviation is a more discriminative feature than calibrated amplitude. Referring to Fig. 5 and Table IV, pulse deviation shows higher mean and standard deviation for grass and tree canopy than other classes due to the spatial distribution of those targets in the path of the laser beam, making it a relatively strong feature for discriminating those classes from the others.

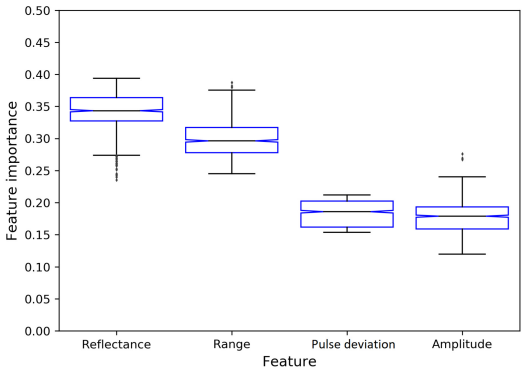

Fig. 6. Feature importance from RF classifier trained on online waveform feature vectors.

Fig. 6 illustrates the importance of each feature in the online waveform feature vectors, from the October training set, reported by the RF classifier. Using a boxplot to show feature importance also gives visual information about the distribution of features in the feature vector. As predicted earlier, the relative reflectance has the highest importance for classification based on the online waveform feature vector. The lower importance of the amplitude with respect to the range is partly due to the fact that the pulse amplitude is not compensated for range.

Amplitude has the lowest discriminative capability in this classification experiment. However, the amplitude's mean and standard deviation given in Table IV and its density distribution plot shown in Fig. 5, shows a degree of power for separating asphalt and tree canopy from grass instances.

The classification results for the online waveform feature vectors from the October test set, including and excluding the range attribute, using the RF classifier and the proposed DCNN-based classifier are given in Tables V and VI, respectively. Each table summarizes the performance of the underlying classifier using the confusion matrix, precision, recall, and F1-score for each individual target category. Furthermore, the weighted average of those metrics has also been reported, where the average metrics take into account the imbalance of the test set. According to Tables V and VI, the overall classification accuracy reported from the RF classifier is comparable with that from DCNN model. In addition, excluding the range attribute from the online waveform feature vectors caused a decrease in the overall accuracy of about 3% for both classifiers. Both classifiers show similar performance in discriminating different target categories based on their online waveform features.

TABLE V

RF-BASED CLASSIFICATION PERFORMANCE FOR ONLINE WAVEFORM FEATURES FROM THE OCTOBER TEST SET. THE VALUES ABOVE AND BELOW THE HORIZONTAL LINES SHOW THE RESULTS FOR ONLINE FEATURE VECTORS INCLUDING AND EXCLUDING THE RANGE VALUES, RESPECTIVELY

Reference points	Classified points: Asphalt	Building	Grass	Tree trunk	Tree canopy	Precision	Recall	F1-score
Asphalt	$\frac{0.80}{0.78}$	$\frac{0.01}{0.01}$	$\frac{0.07}{0.07}$	$\frac{0.00}{0.00}$	$\frac{0.13}{0.15}$	$\frac{0.72}{0.71}$	$\frac{0.80}{0.78}$	$\frac{0.75}{0.74}$
Building	$\frac{0.01}{0.01}$	$\frac{0.80}{0.75}$	$\frac{0.03}{0.04}$	$\frac{0.13}{0.17}$	$\frac{0.03}{0.04}$	$\frac{0.82}{0.76}$	$\frac{0.80}{0.75}$	$\frac{0.81}{0.75}$
Grass	$\frac{0.08}{0.08}$	$\frac{0.06}{0.06}$	$\frac{0.76}{0.75}$	$\frac{0.03}{0.04}$	$\frac{0.07}{0.07}$	$\frac{0.77}{0.76}$	$\frac{0.76}{0.75}$	$\frac{0.77}{0.75}$
Tree trunk	$\frac{0.00}{0.00}$	$\frac{0.11}{0.18}$	$\frac{0.04}{0.04}$	$\frac{0.84}{0.76}$	$\frac{0.01}{0.01}$	$\frac{0.82}{0.76}$	$\frac{0.84}{0.76}$	$\frac{0.83}{0.76}$
Tree canopy	$\frac{0.22}{0.22}$	$\frac{0.02}{0.02}$	$\frac{0.09}{0.10}$	$\frac{0.01}{0.01}$	$\frac{0.66}{0.65}$	$\frac{0.73}{0.71}$	$\frac{0.66}{0.65}$	$\frac{0.69}{0.68}$
Weighted average						$\frac{0.77}{0.74}$	$\frac{0.77}{0.74}$	$\frac{0.77}{0.74}$
Overall accuracy	$\frac{77\%}{74\%}$							

TABLE VI

DCNN-BASED CLASSIFICATION PERFORMANCE FOR ONLINE WAVEFORM FEATURES FROM THE OCTOBER TEST SET. THE VALUES ABOVE AND BELOW THE HORIZONTAL LINES SHOW THE RESULTS FOR ONLINE FEATURE VECTORS INCLUDING AND EXCLUDING THE RANGE VALUES, RESPECTIVELY

Reference points	Classified points: Asphalt	Building	Grass	Tree trunk	Tree canopy	Precision	Recall	F1-score
Asphalt	$\frac{0.85}{0.85}$	$\frac{0.00}{0.00}$	$\frac{0.06}{0.06}$	$\frac{0.00}{0.00}$	$\frac{0.09}{0.08}$	$\frac{0.70}{0.70}$	$\frac{0.85}{0.85}$	$\frac{0.77}{0.77}$
Building	$\frac{0.01}{0.01}$	$\frac{0.79}{0.76}$	$\frac{0.02}{0.03}$	$\frac{0.14}{0.17}$	$\frac{0.04}{0.04}$	$\frac{0.81}{0.68}$	$\frac{0.79}{0.76}$	$\frac{0.80}{0.72}$
Grass	$\frac{0.09}{0.08}$	$\frac{0.06}{0.06}$	$\frac{0.76}{0.77}$	$\frac{0.03}{0.03}$	$\frac{0.06}{0.05}$	$\frac{0.79}{0.76}$	$\frac{0.76}{0.77}$	$\frac{0.77}{0.77}$
Tree trunk	$\frac{0.00}{0.00}$	$\frac{0.12}{0.30}$	$\frac{0.04}{0.05}$	$\frac{0.83}{0.63}$	$\frac{0.01}{0.01}$	$\frac{0.81}{0.73}$	$\frac{0.83}{0.63}$	$\frac{0.82}{0.68}$
Tree canopy	$\frac{0.26}{0.26}$	$\frac{0.02}{0.02}$	$\frac{0.09}{0.10}$	$\frac{0.01}{0.01}$	$\frac{0.63}{0.61}$	$\frac{0.76}{0.76}$	$\frac{0.63}{0.61}$	$\frac{0.69}{0.68}$
Weighted average						$\frac{0.76}{0.73}$	$\frac{0.77}{0.73}$	$\frac{0.77}{0.73}$
Overall accuracy	$\frac{77\%}{73\%}$							

Misclassified instances resulting from the classification of online waveform feature vectors, including and excluding the range attribute, follow the same pattern in Tables V and VI. According to the F1-score values, both classifiers show the highest performance on building and tree trunk categories. However, they show a lower skill in detecting tree canopy instances. According to the confusion matrices given in Tables V and VI, tree canopy has the highest rate of misclassified instances with asphalt. This observation was predictable by referring to the reflectance distribution plot given in Fig. 5, where reflectance distributions for the asphalt and tree canopy classes shows the largest overlap. Buildings, on the other hand, shows the highest misclassified instances with tree trunk, which was, also, predictable by examining the plots in Fig. 5. In addition, referring to the confusion matrices, the grass category has about 25% misclassified instances which are distributed among other target categories.

It is worth noting that the significant difference between precision and recall for asphalt in both classifiers, given in Tables V and VI, shows that despite the relatively large number of misclassified instances of asphalt in other classes, notably tree canopy and grass, both classifiers are still able to correctly detect a large portion of asphalt returns. Conversely, the relatively higher precision than recall for tree canopy class derived from both classification methods shows that the underlying classifier is more skillful in detecting instances that do not belong to the tree canopy than detecting instances that do actually belong to that class. The above classification results are consistent with the information retrieved from the feature distribution and feature importance plots given in Figs. 5 and 6, respectively.

B. Built Environment Classification Using Offline Waveform Features From the October Test Set

Fig. 7 illustrates the feature importance plot reported by the RF classifier for training based on the offline waveform feature vectors related to the targets measured for the campus study site. S_1 to S_{24} in horizontal axis of the plot show sample indices for the measured waveforms. According to the

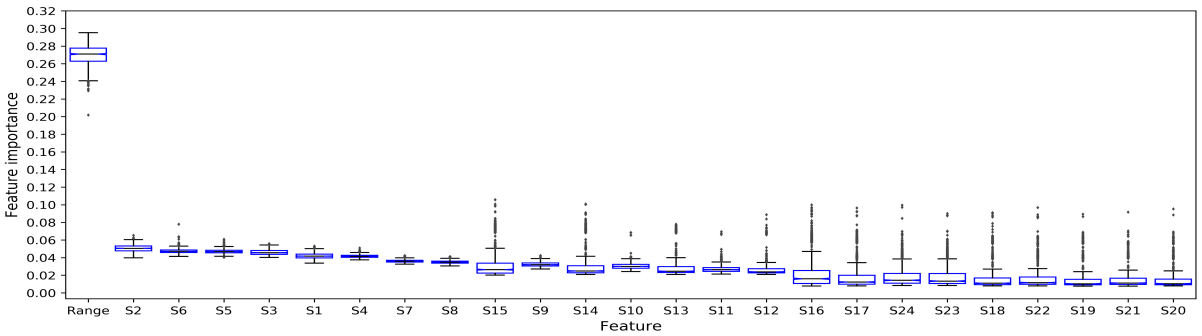

Fig. 7. Feature importance from the RF classifier trained using offline waveform feature vectors.

TABLE VII

RF-BASED CLASSIFICATION PERFORMANCE FOR OFFLINE WAVEFORM FEATURES FROM THE OCTOBER TEST SET. THE VALUES ABOVE AND BELOW THE HORIZONTAL LINES SHOW THE RESULTS FOR ONLINE FEATURE VECTORS INCLUDING AND EXCLUDING THE RANGE VALUES, RESPECTIVELY

Reference points	Classified points: Asphalt	Building	Grass	Tree trunk	Tree canopy	Precision	Recall	F1-score
Asphalt	0.89 0.81	0.00 0.05	0.04 0.03	0.00 0.05	0.07 0.06	0.82 0.64	0.89 0.81	0.85 0.72
Building	0.01 0.12	0.80 0.67	0.02 0.01	0.13 0.16	0.04 0.04	0.76 0.59	0.80 0.67	0.78 0.63
Grass	0.05 0.09	0.04 0.03	0.82 0.75	0.03 0.04	0.06 0.09	0.83 0.82	0.82 0.75	0.82 0.79
Tree trunk	0.00 0.14	0.22 0.33	0.03 0.03	0.73 0.44	0.02 0.06	0.79 0.55	0.73 0.43	0.76 0.78
Tree canopy	0.12 0.11	0.01 0.07	0.07 0.10	0.01 0.07	0.79 0.65	0.81 0.72	0.79 0.65	0.80 0.68
Weighted average						0.80 0.67	0.80 0.66	0.80 0.66
Overall accuracy	80% 67%							

plot, the range to the target has the highest importance for classification. This was predictable due to the high correlation between the intensity (amplitude) of the echo signal and the range to the target. Referring to Fig. 7, it is interesting to note that waveform samples related to the rise time and fall time of the return waveform, which usually happen around samples $S2$ and $S6$, respectively, in the single-peak echo waveforms measured by the Riegl VZ-400 TLS system, are more important than other samples. Furthermore, according to the plot, samples representing the rise time and fall-time of the signal are almost equally important, with samples closely representing the amplitude of the echo waveform. Analyzing the DNs for all recorded waveforms indicates that the peak of the echo signal usually occurs somewhere between the $S4$ and $S6$ samples. This observation confirms the importance of rise time and fall time of the echo waveform for classification in [24], where the authors highlight the importance of those features in the waveform feature vector for discriminating different tree types.

According to Fig. 7, waveform samples S_1–S_8 follow a symmetric distribution with a limited range of outliers, whereas the majority of samples related to the falling tail of the waveform, S_9–S_{24} follow asymmetric, positively skewed distributions with a larger range of outliers, which makes them less important features for efficiently training the classifier. In other words, samples related to the falling tail of the waveform carry less discriminative information for target classification.

The classification results for the offline waveform feature vectors from the October test set, including and excluding range, using the RF classified and the proposed DCNN-based classifier are given in Tables VII and VIII, respectively. According to those tables and considering Tables V and VI, which shows classification results of the online waveform feature vectors, the overall classification accuracy on the offline waveform feature vectors is 3% higher than that for the online waveform feature vectors, when the RF classifier is used for classification. However, the classification results on the offline waveform feature vectors using the DCNN-based classifier show a noticeable improvement of 10% in overall accuracy relative to the RF and DCNN-based classification performance using online waveform feature vectors. In addition, referring to Table VII, excluding range from the offline waveform feature vector reduces the performance of the RF by 13%, while this reduction, according to Table VIII, is about 7% for classification based on the DCNN model.

Comparing Tables VII and VIII (offline waveform features) with Tables V and VI (online waveform features) shows a relatively similar pattern for misclassified class instances. Moreover, exploring the classification performance of the DCNN for each individual target category using online and

TABLE VIII

DCNN-BASED CLASSIFICATION PERFORMANCE FOR OFFLINE WAVEFORM FEATURES FROM THE OCTOBER TEST SET. THE VALUES ABOVE AND BELOW THE HORIZONTAL LINES SHOW THE RESULTS FOR ONLINE FEATURE VECTORS INCLUDING AND EXCLUDING THE RANGE VALUES, RESPECTIVELY

	Classified points							
Reference points	Asphalt	Building	Grass	Tree trunk	Tree canopy	Precision	Recall	F1-score
Asphalt	$\frac{0.94}{0.87}$	$\frac{0.00}{0.05}$	$\frac{0.02}{0.03}$	$\frac{0.00}{0.02}$	$\frac{0.04}{0.03}$	$\frac{0.89}{0.73}$	$\frac{0.94}{0.87}$	$\frac{0.91}{0.80}$
Building	$\frac{0.01}{0.07}$	$\frac{0.89}{0.82}$	$\frac{0.01}{0.01}$	$\frac{0.07}{0.05}$	$\frac{0.02}{0.05}$	$\frac{0.80}{0.60}$	$\frac{0.89}{0.82}$	$\frac{0.84}{0.69}$
Grass	$\frac{0.04}{0.08}$	$\frac{0.02}{0.02}$	$\frac{0.88}{0.83}$	$\frac{0.02}{0.02}$	$\frac{0.04}{0.06}$	$\frac{0.89}{0.85}$	$\frac{0.88}{0.83}$	$\frac{0.88}{0.84}$
Tree trunk	$\frac{0.00}{0.09}$	$\frac{0.17}{0.40}$	$\frac{0.02}{0.03}$	$\frac{0.80}{0.42}$	$\frac{0.01}{0.06}$	$\frac{0.83}{0.77}$	$\frac{0.80}{0.42}$	$\frac{0.82}{0.54}$
Tree canopy	$\frac{0.06}{0.08}$	$\frac{0.02}{0.08}$	$\frac{0.06}{0.07}$	$\frac{0.00}{0.04}$	$\frac{0.86}{0.74}$	$\frac{0.87}{0.78}$	$\frac{0.86}{0.74}$	$\frac{0.87}{0.76}$
Weighted average						$\frac{0.86}{0.75}$	$\frac{0.87}{0.74}$	$\frac{0.87}{0.74}$
Overall accuracy	$\frac{87\%}{74\%}$							

TABLE IX

DCNN-BASED CLASSIFICATION PERFORMANCE FOR THE JULY TEST SET. THE VALUES ABOVE AND BELOW THE HORIZONTAL LINES SHOW THE RESULTS FOR OFFLINE AND ONLINE FEATURE VECTOR CLASSIFICATION, RESPECTIVELY

	Classified points							
Reference points	Asphalt	Building	Grass	Tree trunk	Tree canopy	Precision	Recall	F1-score
Asphalt	$\frac{0.81}{0.89}$	$\frac{0.07}{0.00}$	$\frac{0.01}{0.01}$	$\frac{0.00}{0.00}$	$\frac{0.11}{0.10}$	$\frac{0.86}{0.64}$	$\frac{0.81}{0.89}$	$\frac{0.84}{0.74}$
Building	$\frac{0.00}{0.00}$	$\frac{0.81}{0.59}$	$\frac{0.00}{0.00}$	$\frac{0.15}{0.35}$	$\frac{0.04}{0.05}$	$\frac{0.69}{0.69}$	$\frac{0.81}{0.59}$	$\frac{0.75}{0.64}$
Grass	$\frac{0.09}{0.16}$	$\frac{0.07}{0.04}$	$\frac{0.78}{0.64}$	$\frac{0.00}{0.01}$	$\frac{0.06}{0.16}$	$\frac{0.87}{0.83}$	$\frac{0.78}{0.64}$	$\frac{0.83}{0.72}$
Tree trunk	$\frac{0.00}{0.01}$	$\frac{0.36}{0.41}$	$\frac{0.04}{0.05}$	$\frac{0.58}{0.51}$	$\frac{0.02}{0.01}$	$\frac{0.87}{0.42}$	$\frac{0.59}{0.51}$	$\frac{0.71}{0.46}$
Tree canopy	$\frac{0.14}{0.35}$	$\frac{0.02}{0.02}$	$\frac{0.08}{0.09}$	$\frac{0.00}{0.00}$	$\frac{0.76}{0.53}$	$\frac{0.85}{0.63}$	$\frac{0.77}{0.53}$	$\frac{0.80}{0.58}$
Weighted average						$\frac{0.82}{0.64}$	$\frac{0.81}{0.63}$	$\frac{0.81}{0.63}$
Overall accuracy	$\frac{80\%}{65\%}$							

offline waveform feature vectors as reported in Tables VI and VIII, respectively, shows that classification based on the samples of the raw waveform significantly improves classification performance across almost all classes. One reason for this improvement might be due to the capability of DCNN models in exploring and discovering a hierarchy of complicated features from input data which are more discriminative than input attributes to the classifier.

Interestingly, the RF and DCNN-based classification results for the tree trunk category shown in Tables V and VI (online waveform features) when compared to results shown in Tables VII and VIII (offline waveform features) reveals that higher classification performance can be achieved for this target category using the online waveform features rather than the raw waveform samples. Referring to the reflectance distribution plot given in Fig. 5, this may be due to the relatively narrow distribution of the calibrated reflectance attribute related to tree trunks that may help the underlying classifier more effectively detect instances in that category.

C. Built Environment Classification Using Online/Offline Waveform Features From the July Test Set

The classification results for both online and offline waveform feature vectors from the July test set using the DCNN-based classifier is given in Table IX. According to the table the overall accuracy of the classification on offline waveform features is 15% higher than that for the online waveform features.

Considering the F1-scores given in Table IX and comparing those values with equivalent values given in Tables VI and VIII confirm that discrepancies in the raw waveforms collected at two different points in time from the same targets have relatively less impact on the classification performance than differences in the online waveform attributes related to similar targets. The drop in the classification performance over natural targets can be partly due to the impact of seasonal changes on some properties of those targets, where, for example, green and dry grass or tree canopy represent changing backscattering properties. Moreover, atmospheric attenuation factors on the laser energy, such as the humidity index, air pressure, and

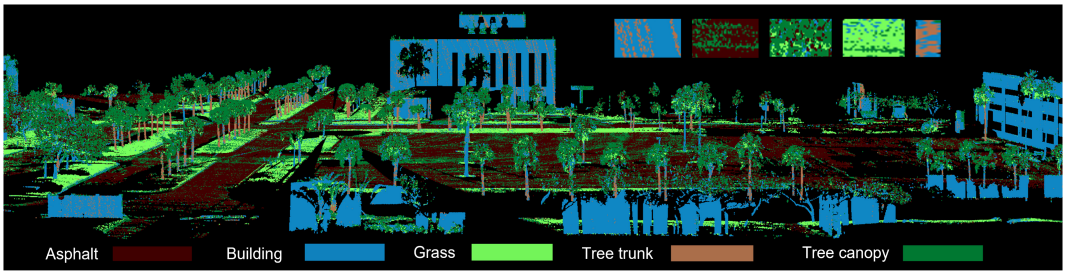

(a)

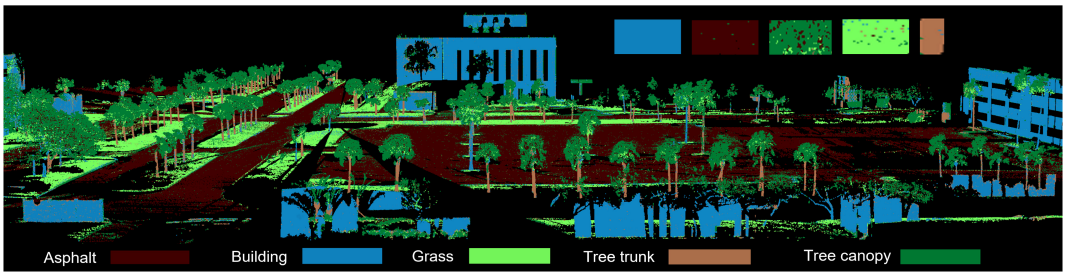

(b)

Fig. 8. Qualification of DCNN-based classification on October test data acquired over the campus study area. Also, five sample areas in classified data, related to five target categories, have been magnified for better visualization of misclassified points. (a) Online waveform. (b) Offline waveform.

TABLE X

DCNN-BASED CLASSIFICATION PERFORMANCE ON THE COASTAL WETLAND AREA. THE VALUES ABOVE AND BELOW THE HORIZONTAL LINES SHOW THE RESULTS FOR OFFLINE AND ONLINE FEATURE VECTOR CLASSIFICATION, RESPECTIVELY

Reference points	Classified points: Tidal flat	Vegetation	Road	Power line	Precision	Recall	F1-score
Tidal flat	$\frac{0.98}{0.97}$	$\frac{0.01}{0.02}$	$\frac{0.01}{0.01}$	$\frac{0.00}{0.00}$	$\frac{0.92}{0.81}$	$\frac{0.98}{0.97}$	$\frac{0.95}{0.88}$
Vegetation	$\frac{0.01}{0.04}$	$\frac{0.98}{0.95}$	$\frac{0.00}{0.01}$	$\frac{0.01}{0.01}$	$\frac{0.95}{0.80}$	$\frac{0.98}{0.95}$	$\frac{0.97}{0.87}$
Road	$\frac{0.12}{0.36}$	$\frac{0.00}{0.40}$	$\frac{0.87}{0.24}$	$\frac{0.00}{0.00}$	$\frac{0.97}{0.89}$	$\frac{0.87}{0.24}$	$\frac{0.92}{0.38}$
Power line	$\frac{0.09}{0.19}$	$\frac{0.15}{0.20}$	$\frac{0.00}{0.01}$	$\frac{0.76}{0.60}$	$\frac{0.96}{0.95}$	$\frac{0.76}{0.60}$	$\frac{0.85}{0.74}$
Weighted average					$\frac{0.95}{0.83}$	$\frac{0.95}{0.82}$	$\frac{0.94}{0.79}$
Overall accuracy	$\frac{95\%}{82\%}$						

temperature, related to each collected dataset may contribute to the related echo waveforms and subsequently derived online waveform attributes, resulting in different misclassification rates in one dataset relative to the other.

Finally, Fig. 8 illustrates the qualification of the classification performance achieved based on the proposed DCNN architecture for both the online and offline waveform data from the October test set. According to the figure, it is clear that the misclassified building and tree trunk instances in the online waveform classification are higher than the offline waveform classification. Also, the higher rate of misclassified instances for asphalt and tree canopy in the online waveform classification can be seen in Fig. 8.

D. Natural Environment Classification

The performance of the proposed DCNN-based classifier on both online and offline waveform feature vectors derived from the TLS survey over the coastal wetland study site is given in Table X. According to the table, the overall accuracy of the multiclass classification for the coastal wetland using the proposed DCNN model on offline waveform feature vectors is 13% higher than that for the online waveform feature vectors. The F1-score reported in Table X, shows that the classification performance on online and offline feature vectors related to both tidal flat and vegetation are more comparable than the performance for the road and power line classes. The calibrated reflectance feature in the tidal flat areas and vegetation areas shows that this online waveform attribute can easily discriminate a large number of instances belonging to those categories. The higher performance of the classification based on the raw waveform samples relative to the online waveform attributes is more noticeable for the road and power line categories. The road class at this study site is comprised of dirt and sediment, similar in composition to the upland less submerged parts of the tidal flat area, making these two areas

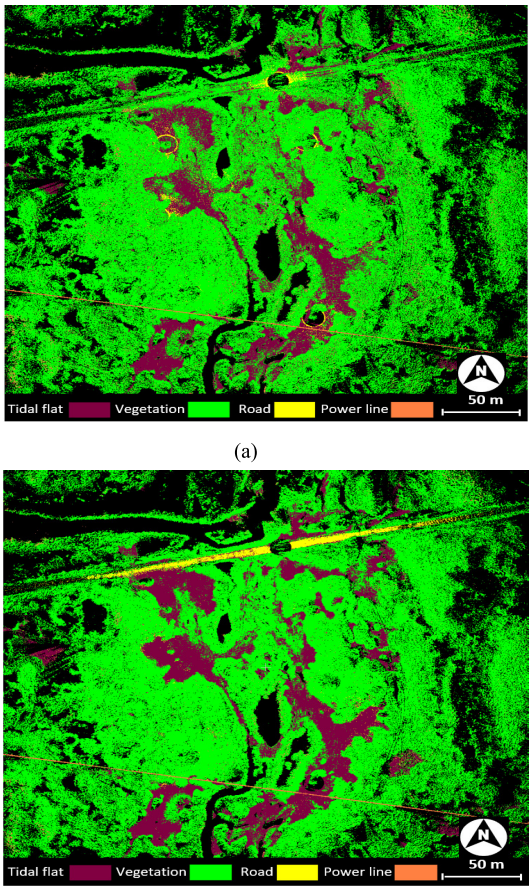

Fig. 9. Qualification of the classification over the study area using online and offline waveform feature vectors. (a) Online waveform. (b) Offline waveform.

challenging for classification. As observed in Table X, classification of the road based on the offline waveform features had a significantly higher classification accuracy compared to classification of the road based on the online waveform features (92% F1-score versus 36%, respectively). According to the confusion matrix results there are large number of misclassified instances with other target categories for online waveform features. Although instances related to the tidal flat and road show very close calibrated reflectance values in their online waveform feature vectors, results suggest that samples of the raw waveform significantly improved discrimination of those two target categories, perhaps due to differences in surface roughness. The qualitative results of the DCNN-based classification for both the online and offline waveform feature vectors are given in Fig. 9.

E. Terrain Surface Modeling for the Coastal Wetland Study Site

The classified points based on both online and offline waveform features are used to approximate terrain models (DTMs) for the coastal wetland study site. Classified points are filtered based on their predicted labels from the proposed DCNN classifier, where the ground points refer to the set of points predicted as road or tidal flat areas. Recall the tidal flat class

TABLE XI

STATISTICS OF VERTICAL ERROR (M) BETWEEN RIEGL VZ-2000I TLS MEASUREMENTS AND RTK GNSS POINTS COLLECTED ON HARD SURFACES AND VEGETATED SURFACES BEFORE AND AFTER APPLYING PMF

		before PMF	after PMF
Statistics (m)	$\Delta Z^{\text{TLS}-\text{GNSS}}_{\text{Hard surfaces}}$	$\Delta Z^{\text{TLS}-\text{GNSS}}_{\text{Vegetated surfaces}}$	$\Delta Z^{\text{TLS}-\text{GNSS}}_{\text{Vegetated surfaces}}$
Mean	0.009	0.116	0.028
Min	−0.017	−0.029	−0.020
Max	0.049	0.711	0.130
StDev	0.019	0.159	0.062
RMSE_Z	0.021	0.197	0.068

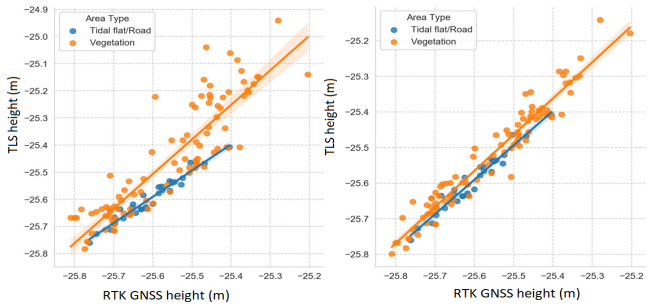

Fig. 10. Scatterplot of RTK GNSS ellipsoid heights versus TLS ellipsoid heights on hard surfaces and vegetated surfaces (Left) before and (Right) after applying PMF.

includes exposed, lower lying and tidal inundated wetland surface areas and upland, periodically inundated wetland surface areas in proximity to sparse or dense vegetation. To evaluate the fidelity of DTMs generated from the DCNN-based filtering result with online and offline waveform features, a classified set of ground points output from the PMF filter applied to the original TLS point cloud is used.

The vertical differences between the RTK GNSS points collected on the exposed wetland/tidal flat surfaces and road surfaces, here called hard surfaces for brevity, and a local TIN model constructed from the original TLS points shows a bias of +0.009 m, which is in the range of the vertical accuracy of the RTK GNSS survey method employed. Table XI reports vertical accuracy statistics for the TLS data relative to the RTK GNSS points collected over hard surfaces and vegetated surfaces, both dense and sparsely vegetated, before and after applying PMF filtering. In addition, the scatterplot for the RTK GNSS ellipsoid heights compared to the TLS measured ellipsoid heights on hard surfaces and vegetated surfaces before and after applying PMF filtering are shown in Fig. 10. The goodness-of-fit or coefficient of determination, r^2, is 0.95 for regression lines related to the hard surfaces in both plots. Whereas, the r^2 coefficient is 0.81 and 0.92 for the regression lines representing the height difference over vegetated surfaces before and after applying PMF, respectively.

The statistics given in Table XI and plot in Fig. 10, clearly show that the vegetated areas can cause a significant bias in the process of modeling the terrain surface, as expected. Moreover, statistics and regression plots given in Table XI and Fig. 10, respectively, show the high performance of the PMF algorithm

TABLE XII

STATISTICS OF VERTICAL DISTANCE (M) BETWEEN TIN SURFACE CONSTRUCTED ON TERRAIN POINTS DERIVED FROM PMF AND CLASSIFIED TERRAIN POINTS, INCLUDING TIDAL FLAT AND ROAD, DERIVED FROM DCNN-BASED CLASSIFICATION ON OFFLINE AND ONLINE WAVEFORM FEATURE VECTORS

Statistics (m)	$DTM^{Offline} - DTM^{PMF}$	$DTM^{Online} - DTM^{PMF}$
Mean	0.000	0.004
Min	−0.020	−0.090
Max	0.212	0.430
StDev	0.005	0.040
$RMSE_Z$	0.005	0.040

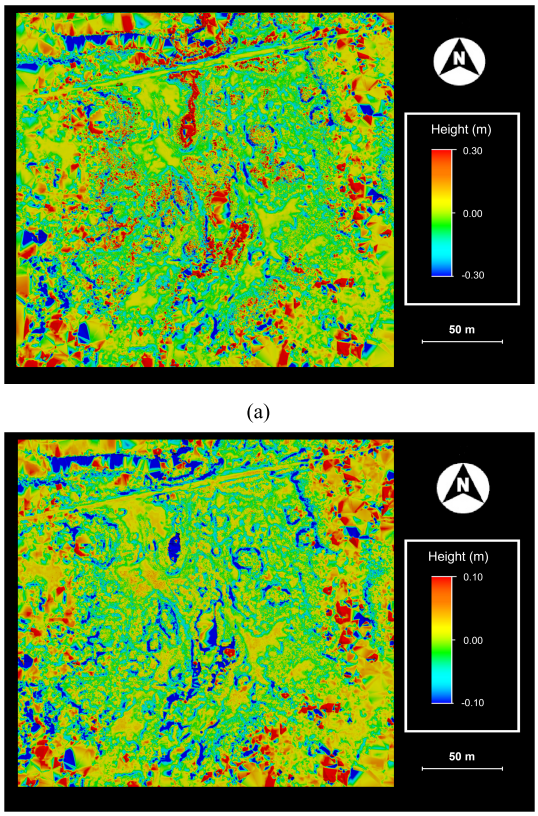

Fig. 11. Differential DTMs computed by subtracting the DCNN-based DTM, computed from online and offline waveform features, from the PMF-based DTM. (a) $DTM^{Online} - DTM^{PMF}$. (b) $DTM^{Offline} - DTM^{PMF}$.

in filtering the above-ground targets and identifying the ground points in the vegetated areas. This justifies the use of the PMF filtering solution as a representative ground point set for evaluating performance of the DCNN-based classification of hard surfaces (tidal flat areas and road areas) using online and offline waveform feature vectors.

Table XII summarizes statistics related to the vertical distance between a TIN surface model constructed from the PMF ground point set, using LAStools (rapidlasso GmbH) point cloud processing software, and the classified point set on hard surfaces resulting from the DCNN-based classification of both the online and offline waveform feature vectors. According to the table, predicted tidal flat and road points from offline waveform features can model the terrain surface with the uncertainty of about one order of magnitude lower than that from predicted points based on the online waveform features.

Fig. 11 shows the differences between a DTM generated from the PMF ground point set and DTMs generated from the DCNN-based classified points on hard surfaces, including tidal flat and road areas, using online and offline waveform feature vectors. All DTMs have been generated using LAStools software with a given step size (resolution) of 0.1 m in both X- and Y-directions. The DTM generated from the offline waveform classification result more closely approximates the DTM generated from the PMF ground point set for both densely vegetated areas, in the middle and upper part of the figure, and sparse vegetation areas on the left and right side of the figure. According to Fig. 11, the range of uncertainty in terrain height on classified tidal flat and road resulted from the online waveform features is significantly higher than that from the offline waveform features. The main reason for the higher vertical uncertainty for classified points from the online waveform features relative to the offline waveform features is the higher rate of misclassified instances of vegetation with tidal flat in the classification based on the online waveform features which results in lower precision value for the tidal flat category. Also, the larger rate of misclassification between tidal flat and vegetation instances in online waveform classification caused a higher vertical uncertainty over the vegetated areas.

VII. CONCLUSION

In this study, the potential of the raw samples of TLS single-peak echo waveforms versus calibrated waveform features from online waveform processing, were explored for point cloud classification within built and natural environments. FW data were collected by the Riegl VZ-Line FW TLS systems in multiple scan positions in each study area, where in addition to the 3D coordinates for each measurement, the calibrated waveform features, from the online waveform processing, and equivalent digitized waveform data were recorded. Also, a DCNN-based classifier was proposed for both online and offline waveform feature vector classification, where its performance was compared with the performance achieved based on RF classification on the same datasets, and feature importance in each feature vector (online versus offline) was reported. This experiment showed that the samples of the digitized waveform can be more discriminative for certain target classes than the limited number of calibrated waveform features from online waveform processing, which resulted in higher overall classification performance. Furthermore, the classification performance on two separate test sets confirms that the offline waveform feature vectors are more stable than the online waveform feature vectors over time.

Results for the selected wetland environment showed that the classification based on samples of the raw waveform outperforms that on the calibrated waveform features. In addition, a filtering procedure to discriminate terrain points based on the predicted label for TLS measurements is more accurate when the classified dataset derived from a raw waveform classification rather than classifying using calibrated waveform features.

The approach for FW TLS data classification based on the raw waveform samples proposed in this work is adaptable to FW airborne lidar and other modalities. The approach is especially useful when the lidar system response for modeling the waveform is complicated or unknown. It is also advantageous where, due to a low sampling rate of the digitizer such as is common in FW TLS systems, accurate modeling of the waveform signal may not be practically feasible.

Some limitations related to the proposed point cloud classification approach should be kept in mind. This approach uses only single-peak echo waveforms for classification. Moreover, the proposed DCNN model has a relatively simple architecture for feature encoding. In addition, to have a more accurate assessment on the potential of the proposed classification approach, it should be evaluated on more complex built and natural environments with more target categories. Substantial variations of the returned waveforms and consequently the derived cross section (calibrated reflectance) values over distances shorter than range resolution, as an inherent limitation of any lidar system (TLS or ALS), should also be considered when interpreting the lidar data or classification performance over complex environments.

As future work, combining online and offline waveform attributes in a more advanced DCNN-based architecture may be explored to more effectively investigate waveform feature space for higher classification performance. Classification of multi-echo waveforms may also be considered as future work. The capability of the proposed classification approach will also be assessed on more complex built and natural environments with more sophisticated target categories. In addition, the proposed raw waveform classification approach can be employed for advanced target identification and filtering procedures in complex environments where the inclusion of geometric information to the feature vector of each individual measurement can boost the performance of the FW lidar data analysis.

ACKNOWLEDGMENT

The statements, findings, conclusions, and recommendations are those of the author(s) and do not necessarily reflect the views of the National Oceanic and Atmospheric Administration of the U.S. Department of Commerce.

REFERENCES

[1] A. Guarnieri, F. Pirotti, and A. Vettore, "Comparison of discrete return and waveform terrestrial laser scanning for dense vegetation filtering," *Int. Arch. Photogramm., Remote Sens. Spatial Inf. Sci.*, vol. B7, pp. 511–516, Aug. 2012.

[2] A. Ullrich and M. Pfennigbauer, "Echo digitization and waveform analysis in airborne and terrestrial laser scanning," *Photogramm. Week*, vol. 11, pp. 217–228, Sep. 2011.

[3] W. Wagner, "Radiometric calibration of small-footprint full-waveform airborne laser scanner measurements: Basic physical concepts," *ISPRS J. Photogramm. Remote Sens.*, vol. 65, no. 6, pp. 505–513, Nov. 2010.

[4] C. Mallet and F. Bretar, "Full-waveform topographic LiDAR: State-of-the-art," *ISPRS J. Photogramm. Remote Sens.*, vol. 64, no. 1, pp. 1–16, Jan. 2009.

[5] B. Höfle, M. Hollaus, and J. Hagenauer, "Urban vegetation detection using radiometrically calibrated small-footprint full-waveform airborne LiDAR data," *ISPRS J. Photogramm. Remote Sens.*, vol. 67, pp. 134–147, Jan. 2012.

[6] J. Reitberger, P. Krzystek, and U. Stilla, "Analysis of full waveform LiDAR data for the classification of deciduous and coniferous trees," *Int. J. Remote Sens.*, vol. 29, no. 5, pp. 1407–1431, Mar. 2008.

[7] B. Jutzi and U. Stilla, "Range determination with waveform recording laser systems using a Wiener filter," *ISPRS-J. Photogramm. Remote Sens.*, vol. 61, no. 2, pp. 95–107, Nov. 2006.

[8] P. J. Hartzell, C. L. Glennie, and D. C. Finnegan, "Empirical waveform decomposition and radiometric calibration of a terrestrial full-waveform laser scanner," *IEEE Trans. Geosci. Remote Sens.*, vol. 53, no. 1, pp. 162–172, Jan. 2014.

[9] M. Pfennigbauer and A. Ullrich, "Improving quality of laser scanning data acquisition through calibrated amplitude and pulse deviation measurement," *Proc. SPIE*, vol. 7684, Apr. 2010, Art. no. 76841F.

[10] C. E. Parrish, I. Jeong, R. D. Nowak, and R. B. Smith, "Empirical comparison of full-waveform LiDAR algorithms," *Photogramm. Eng. Remote Sens.*, vol. 77, no. 8, pp. 825–838, Aug. 2011.

[11] C. Mallet, F. Bretar, and U. Soergel, "Analysis of full-waveform lidar data for classification of urban areas," *Photogram. Fernerkundung Geoinf.*, vol. 5, pp. 337–349, 2008.

[12] C. Alexander, K. Tansey, J. Kaduk, D. Holland, and N. J. Tate, "Backscatter coefficient as an attribute for the classification of full-waveform airborne laser scanning data in urban areas," *ISPRS J. Photogramm. Remote Sens.*, vol. 65, no. 5, pp. 423–432, Sep. 2010.

[13] C. Mallet, F. Bretar, M. Roux, U. Soergel, and C. Heipke, "Relevance assessment of full-waveform LiDAR data for urban area classification," *ISPRS J. Photogramm. Remote Sens.*, vol. 66, no. 6, pp. S71–S84, Dec. 2011.

[14] K. D. Fieber, I. J. Davenport, J. M. Ferryman, R. J. Gurney, J. P. Walker, and J. M. Hacker, "Analysis of full-waveform LiDAR data for classification of an orange orchard scene," *ISPRS J. Photogramm. Remote Sens.*, vol. 82, pp. 63–82, Aug. 2013.

[15] M. Azadbakht, C. S. Fraser, and K. Khoshelham, "Synergy of sampling techniques and ensemble classifiers for classification of urban environments using full-waveform LiDAR data," *Int. J. Appl. Earth Observ. Geoinf.*, vol. 73, pp. 277–291, Dec. 2018.

[16] X. Lai, Y. Yuan, Y. Li, and M. Wang, "Full-waveform LiDAR point clouds classification based on wavelet support vector machine and ensemble learning," *Sensors*, vol. 19, no. 14, p. 3191, Jul. 2019.

[17] L. Ma, M. Zhou, and C. Li, "Land covers classification based on random forest method using features from full-waveform LiDAR data," *Int. Arch. Photogramm., Remote Sens. Spatial Inf. Sci.*, vol. 2/W7, pp. 263–268, Sep. 2017.

[18] M. Bruggisser, A. Roncat, M. E. Schaepman, and F. Morsdorf, "Retrieval of higher order statistical moments from full-waveform LiDAR data for tree species classification," *Remote Sens. Environ.*, vol. 196, pp. 28–41, Jul. 2017.

[19] P. Crespo-Peremarch, R. A. Fournier, V.-T. Nguyen, O. R. van Lier, and L. Á. Ruiz, "A comparative assessment of the vertical distribution of forest components using full-waveform airborne, discrete airborne and discrete terrestrial laser scanning data," *Forest Ecol. Manage.*, vol. 473, Oct. 2020, Art. no. 118268.

[20] D. Chen, J. Peethambaran, and Z. Zhang, "A supervoxel-based vegetation classification via decomposition and modelling of full-waveform airborne laser scanning data," *Int. J. Remote Sens.*, vol. 39, no. 9, pp. 2937–2968, Jan. 2018.

[21] B. Höfle and M. Hollaus, "Urban vegetation detection using high density full-waveform airborne lidar data-combination of object-based image and point cloud analysis," *Int. Arch. Photogramm. Remote Sens. Spat. Inf. Sci.*, vol. 38, pp. 281–286, 2010.

[22] L. Guo, N. Chehata, C. Mallet, and S. Boukir, "Relevance of airborne LiDAR and multispectral image data for urban scene classification using Random Forests," *ISPRS J. Photogramm. Remote Sens.*, vol. 66, no. 1, pp. 56–66, Jan. 2011.

[23] A. Neuenschwander, L. Magruder, and R. Gutierrez, "Signal processing techniques for feature extraction and classification using small-footprint full-waveform airborne LiDAR," in *Proc. IGARSS - IEEE Int. Geosci. Remote Sens. Symp.*, Jul. 2008, pp. III-676–III-679.

[24] A. L. Neuenschwander, "Landcover classification of small-footprint, full-waveform LiDAR data," *J. Appl. Remote Sens.*, vol. 3, no. 1, Aug. 2009, Art. no. 033544.

[25] P. Crespo-peremarch, P. Tompalski, C. C. Nicholas, and L. Ruiz, "Characterizing understory vegetation in Mediterranean forests using full-waveform airborne laser scanning data," *Remote Sens. Environ.*, vol. 217, pp. 400–413, Aug. 2018.

[26] S. Luo *et al.*, "Estimating forest aboveground biomass using small-footprint full-waveform airborne LiDAR data," *Int. J. Appl. Earth Observ. Geoinf.*, vol. 83, Nov. 2019, Art. no. 101922.
[27] M. Doneus, M. Pfennigbauer, N. Studnicka, and A. Ullrich, "Terrestrial waveform laser scanning for documentation of cultural heritage," in *Proc. 22th CIPA Symp.*, Kyoto Japan, 2009, pp. 1–6.
[28] S. Zorzi, E. Maset, A. Fusiello, and F. Crosilla, "Full-waveform airborne LiDAR data classification using convolutional neural networks," *IEEE Trans. Geosci. Remote Sens.*, vol. 57, no. 10, pp. 8255–8261, Oct. 2019.
[29] M. Azadbakht, C. S. Fraser, and K. Khoshelham, "Improved urban scene classification using full-waveform LiDAR," *Photogramm. Eng. Remote Sens.*, vol. 82, no. 12, pp. 973–980, Dec. 2016.
[30] X. Shen, L. Cao, D. Chen, Y. Sun, G. Wang, and H. Ruan, "Prediction of forest structural parameters using airborne full-waveform LiDAR and hyperspectral data in subtropical forests," *Remote Sens.*, vol. 10, no. 11, p. 1729, Nov. 2018.
[31] C. Sun, S. Cao, and G. A. Sanchez-Azofeifa, "Mapping tropical dry forest age using airborne waveform LiDAR and hyperspectral metrics," *Int. J. Appl. Earth Observ. Geoinf.*, vol. 83, Nov. 2019, Art. no. 101908.
[32] S. Kaasalainen *et al.*, "Brightness measurements and calibration with airborne and terrestrial laser scanners," *IEEE Trans. Geosci. Remote Sens.*, vol. 46, no. 2, pp. 528–534, Feb. 2008.
[33] S. Kaasalainen, A. Jaakkola, M. Kaasalainen, A. Krooks, and A. Kukko, "Analysis of incidence angle and distance effects on terrestrial laser scanner intensity: Search for correction methods," *Remote Sens.*, vol. 3, no. 10, pp. 2207–2221, 2011.
[34] Y. Guo, H. Wang, Q. Hu, H. Liu, L. Liu, and M. Bennamoun, "Deep learning for 3D point clouds: A survey," *IEEE Trans. Pattern Anal. Mach. Intell.*, vol. 43, no. 12, pp. 4338–4364, Dec. 2021.
[35] W. Liao, F. Van Coillie, L. Gao, L. Li, B. Zhang, and J. Chanussot, "Deep learning for fusion of APEX hyperspectral and full-waveform LiDAR remote sensing data for tree species mapping," *IEEE Access*, vol. 6, pp. 68716–68729, 2018.
[36] D. P. Kingma and J. Ba, "Adam: A method for stochastic optimization," 2014, *arXiv:1412.6980*.
[37] Y. Jin, X. Liu, Y. Chen, and X. Liang, "Land-cover mapping using random forest classification and incorporating NDVI time-series and texture: A case study of central Shandong," *Int. J. Remote Sens.*, vol. 39, no. 23, pp. 8703–8723, 2018.
[38] K. Zhang, S.-C. Chen, D. Whitman, M.-L. Shyu, J. Yan, and C. Zhang, "A progressive morphological filter for removing nonground measurements from airborne LiDAR data," *IEEE Trans. Geosci. Remote Sens.*, vol. 41, no. 4, pp. 872–882, Apr. 2003.

Mohammad Pashaei (Member, IEEE) received the B.S. degree in civil engineering-surveying from the Amirkabir University of Technology (Tehran Polytechnic), Tehran, Iran, in 2005, the M.S. degree in civil engineering-surveying-photogrammetry from the University of Tehran, Tehran, in 2009, and the Ph.D. degree in geospatial computing science from Texas A&M University at Corpus Christi, Corpus Christi, TX, USA.

He is currently working as a Post-Doctoral Research Fellow with the College of Science and Engineering, Texas A&M University at Corpus Christi. His study and research interests include developing machine learning/deep learning-based framework for information retrieval from remote sensing (RS) data collected by different RS technologies, including UAS and lidar.

Michael J. Starek (Member, IEEE) received the M.S. degree in computer science from Texas A&M University at Corpus Christi, Corpus Christi, TX, USA, and the Ph.D. degree in civil engineering with emphasis in geosensing systems engineering from the University of Florida, Gainesville, FL, USA, in 2009.

From 2009 to 2011, he was a National Research Council Postdoctoral Fellow with the U.S. Army Research Office in affiliation with North Carolina State University, Raleigh, NC, USA, where he continued to work with the Geoinformation Science and Environmental Modeling Laboratory until 2012. From 2014 to 2018, he was an Assistant Professor of geospatial systems engineering with the School of Engineering and Computing Sciences, Texas A&M University at Corpus Christi. In 2018, he was promoted to an Associate Professor. He serves as the Director of the Measurement Analytics Laboratory (MANTIS) and the Chief Scientist of the Conrad Blucher Institute, Texas A&M University at Corpus Christi. His research interests include the merging of geomatics, remote sensing, and geospatial computing/AI.

Craig L. Glennie (Member, IEEE) received the B.Sc. and Ph.D. degrees in geomatics engineering from the University of Calgary, Calgary, AB, Canada.

He is currently an Assistant Professor in civil and environmental engineering with the University of Houston, Houston, TX, USA, and a Co-Principal Investigator with the NSF-funded National Center for Airborne Laser Mapping. He was formerly the Vice President of Engineering for Terrapoint, a lidar remote sensing company with offices in Canada and USA. He has been active in the design, development, and operation of kinematic remote sensing systems for 13 years. He is a registered Professional Engineer in Calgary.

Jacob Berryhill received the B.S. degree in geospatial information systems from Texas A&M University at Corpus Christi, Corpus Christi, TX, USA, in 2016, where he is currently pursuing the M.S. degree in geospatial engineering.

From 2014 to 2019, he was a Research Assistant with the MANTIS Remote Sensing Laboratory, Conrad Blucher Institute, where he is currently a Research Engineer. His research interest includes high-resolution mapping using UAS.